Pedro Henrique Poubel Mendonça Da Silveira[1], Jheison Lopes Dos Santos[2], Alaelson Vieira Gomes[1], And Marcelo Henrique Prado Da Silva[1]*

[1]Graduate Programme in Materials Science and Engineering, Military Institute of Engineering—IME, Praça General Tibúrcio 80, Urca, Rio de Janeiro 22290-270, Brazil, [2]Brazilian Institute of Medicine and Rehabilitation, IBMR, Rio de Janeiro, RJ, Brazil

Scientific paper
ISSN 0351-9465, E-ISSN 2466-2585
https://doi.org/10.62638/ZasMat1403

Zastita Materijala 66 ( ) (2025)

Study of crystallite size and lattice strain by Williamson-Hall analysis in sintered Al_2O_3 - Fe_2O_3 ceramics

ABSTRACT

This study investigates the influence of hematite (Fe_2O_3) as a sintering aid in alumina-based (Al_2O_3) ceramics. Samples with Fe_2O_3 concentrations ranging from 0.5 to 8 wt.% were produced and sintered at 1400 °C. The structural characterization of the samples was carried out using X-ray diffraction (XRD). Crystallite size and lattice strain were calculated by the Debye-Scherrer and Williamson-Hall equations. The results showed that Fe_2O_3 addition fostered crystallite size increase in almost all compositions, leading to a distortion in the Al_2O_3 lattice. Furthermore, the increase in crystallite size resulted in a reduction in dislocation density within the ceramics. This work contributes to a better understanding of the Al_2O_3 – Fe_2O_3 system and its applications in advanced ceramic materials, highlighting the importance of proper composition in ceramics of this compound for optimizing the properties of these materials.

***Keywords**: Al_2O_3, Fe_2O_3, Crystallite size, XRD, Williamson – Hall*

1. INTRODUCTION

Alumina ceramics (Al_2O_3) are widely studied for their exceptional properties, such as dimensional stability, high-temperature resistance, and high hardness, making them suitable for various structural and technological applications [1]. However, alumina's brittle behavior is a significant limitation compared to metals and alloys. As an ionic- covalent solid, alumina lacks plastic deformation under load, causing cracks to propagate without energy dissipation, leading to abrupt failure. This brittleness is exacerbated by defects, notches, or thermal shock. Alumina's strong chemical bonds contribute to its low electrical and thermal conductivity, high melting point, and hardness [2].

Advances in materials science have led to new synthesis and processing methods to enhance alumina's properties and mitigate its limitations. One approach is adding low-melting-point sintering additives to create a liquid phase during sintering, bonding ceramic particles at lower temperatures. This is crucial for alumina, as its pure sintering requires temperatures above 1600 °C, increasing production costs and complexity [3,4].

*Corresponding author: P. H. P. M. Da Silveira
E-mail: pedroo.poubel@gmail.com
Paper received: 12.01.2025.
Paper accepted: 09.04.2025.

Metallic oxides, such as CaO, MgO, Nb_2O_5, and ZrO_2, are commonly used as sintering additives for alumina. These additives create a liquid phase that "wets" ceramic particles, facilitating rearrangement and densification by removing pores [5-13]. In some cases, ternary eutectic compositions generate low-melting-point phases tailored for specific ceramic properties [6].

The Al_2O_3-Fe_2O_3 composite, formed by combining alumina and hematite, has garnered attention due to its applications in sorbents and catalysts [14,15] Alumina is known for its surface acidity, high surface area, mechanical strength, and sintering stability, while hematite offers redox behavior and semiconducting properties [18,19] Combining these oxides enhances mechanical, thermal, and catalytic performance, with high-temperature treatment forming new crystalline phases like $FeAlO_3$. This orthorhombic phase, produced under specific conditions, exhibits properties distinct from its parent oxides [20]

Studies on the Al_2O_3–Fe_2O_3 system have explored phase formation and properties. Muan and Gee[21,22] investigated $FeAlO_3$ formation under varying temperatures and oxygen pressures (PO_2), noting its instability below 1318 °C. $FeAlO_3$ stability increases with higher PO_2, with stabilization temperatures ranging from 1318 to 1495 °C. Further studies characterized its orthorhombic structure[23], coexisting phases[24],

and phase diagrams [25]. Thermodynamic properties indicate $FeAlO_3$ is unstable under high-temperature and pressure conditions.[26]

Few studies have explored alumina's physical and mechanical properties with hematite as a sintering additive. Cai et al.[27] added hematite at 1–5 molar fractions to alumina, pressing discs at 100 MPa and sintering at 1550 °C. Densification reached 89–91%, with flexural strength increasing from 47 MPa at 1 molar fraction to 67 MPa at 5. Silveira et al.[28] combined Fe_2O_3 and Nb_2O_5 in alumina-based ceramics, observing densification, phase formation, and mechanical strength. Sintering at 1400 °C improved properties, with flexural strength rising from 90 MPa to 252 MPa and compressive strength from 529 MPa to 705 MPa at 1–2 wt.% Fe_2O_3. However, higher hematite concentrations reduced densification and strength due to porosity.

In a previous study[29], Fe_2O_3 concentrations of 0.5–8 wt.% were added to alumina, sintered at 1400 °C. Results showed that 4–6 wt.% Fe_2O_3 decreased densification and strength due to porosity, while 0.5–2 wt.% enhanced sintering, increasing densification and mechanical performance. These findings highlight the significant influence of Fe_2O_3 concentration on alumina's final properties.

Characterization of ceramics in the Al_2O_3–Fe_2O_3 system is crucial to understanding additive effects. X-ray diffraction (XRD) identifies and quantifies phases while providing crystallite size and microstrain data. Williamson-Hall analysis, derived from XRD, separates crystallite size and microstrain contributions to peak broadening.[30] This method correlates microstructure with mechanical properties, aiding the understanding of Fe_2O_3's impact on sintering and material performance.[31-33]

This study investigates Fe_2O_3 as a sintering additive in Al_2O_3, focusing on phase formation, crystallite growth, and microstructural changes during sintering. Scherrer calculations and Williamson-Hall analysis elucidate the relationships between sintering and material structure.

2. EXPERIMENTAL PROCEDURE

2.1. Materials

The materials used in the fabrication of ceramic bodies are: α-Al_2O_3 (ρ = 3.96 g/cm³; Alcoa P-913, Brazil), with a particle size of 1μm, glycine (Sigma Aldrich), and iron nitrate (Neon Química, Brazil), employed for the preparation of hematite (Fe_2O_3) powders (ρ = 5.26 g/cm³). Polyethylene glycol (PEG) (Isofar, Brazil) was added to provide mechanical strength to the green bodies.

2.2. Fe_2O_3 Powder Synthesis

The Fe_2O_3 powders were obtained through the spontaneous combustion synthesis method. In this process, ferric nitrate [$Fe(NO_3)_3{\cdot}9H_2O$] was used as the oxidizer, and glycine [NH_2CH_2COOH] as the fuel. This method was similar to the one performed in the study by Cao et al.[34] To prepare the powders, $Fe(NO_3)_3{\cdot}9H_2O$ and NH_2CH_2COOH were dissolved in 150 mL of distilled water and the solution was stirred to achieve a homogeneous mixture. Subsequently, the mixture was poured into a 500 mL beaker and heated to 100 °C. During the heating process, the water in the solution evaporated, transforming the mixture into a gelatinous mass. After a few minutes of heating, the mixture expanded, releasing a significant amount of gases. This was followed by a non-explosive exothermic reaction, resulting in spontaneous combustion. After the burn, a foam composed of iron oxide was obtained, which was crushed to produce the Fe_2O_3 powders used as sintering additives.

2.3. Ceramic Processing

The theoretical density of the samples was determined using the Rule of Mixtures, excluding PEG which is eliminated during sintering. Table 1 presents the theoretical density (TD) values and nomenclature of each sample.

Table 1. Composition, nomenclature and theoretical density of sample groups of this paper

Sample	Composition	Density (g/cm³)
AL	100 wt.% Al_2O_3	3.960
ALFE05	99.5 wt.% Al_2O_3 – 0.5wt.%Fe_2O_3	3.966
ALFE10	99 wt.% Al_2O_3 – 1 wt.% Fe_2O_3	3.973
ALFE20	98 wt.% Al_2O_3 – 2 wt.% Fe_2O_3	3.986
ALFE40	96 wt.% Al_2O_3 – 4 wt.% Fe_2O_3	4.012
ALFE60	94 wt.% Al_2O_3 – 6 wt.% Fe_2O_3	4.038
ALFE80	92 wt.% Al_2O_3 – 8 wt.% Fe_2O_3	4.064

Al_2O_3, Fe_2O_3, and PEG were homogenized in a ball mill for 8h, using distilled water in a 1:1 ratio to facilitate the mixture. After this process, the powders were dried for 48h at a temperature of 120 °C, manually deagglomerated, and sieved through a 60-mesh screen. Using these materials, discs with a diameter of 15 mm and a mass of 0.5 g were produced through cold uniaxial pressing with a load of 50 MPa. Sintering was conducted in a JUNG furnace, without the application of pressure, with a maximum temperature of 1400 °C, followed by inertial cooling. The heating ramp utilized is illustrated in Figure 1.

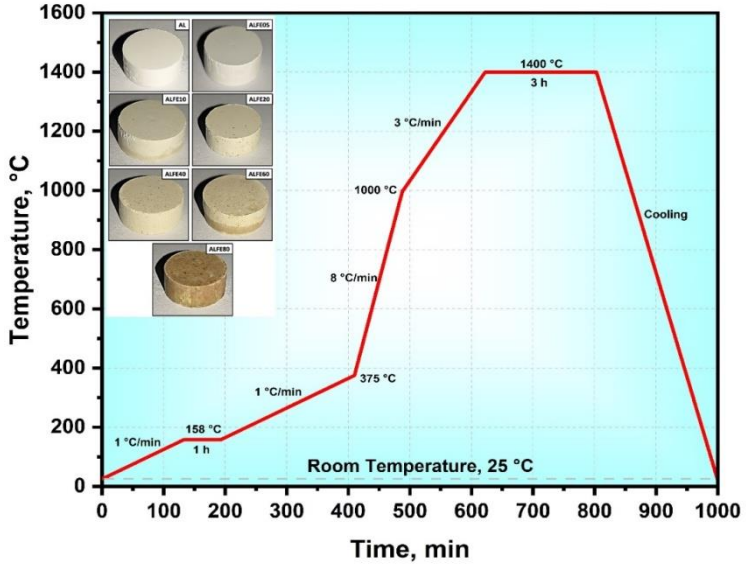

Figure 1. Sintering ramp used for sintering of Al_2O_3 – Fe_2O_3 ceramics. The samples displayed in the graph are the groups of sintered samples

The X-Ray diffraction analysis of the sintered samples was conducted using the X'Pert Pro MRDdiffractometer from Panalytical (São Paulo, Brazil). The scanning range extended from 20° to 90°, with an increment of 0.02° and an acquisition time of 2s. Employing a Co-Kα tube (λ = 1,79 Å), the analysis was carried out with a voltage of 40 Kv and a current of 40 Ma. The qualitative identification of the formed phases was performed using the Panalytical`sHighScore Plus software.

3. RESULTS AND DISCUSSION

3.1. XRD Analysis of Al_2O_3 – Fe_2O_3 Ceramics

Figure 2(a) shows the diffraction patterns of the sintered ceramics with the peaks indexing. The primary identified phase corresponds to α-Al_2O_3 (corundum), a highly stable phase with a rhombohedral crystal structure and space group R-3c, as confirmed by the JCPDS 00-073-1512 reference card.

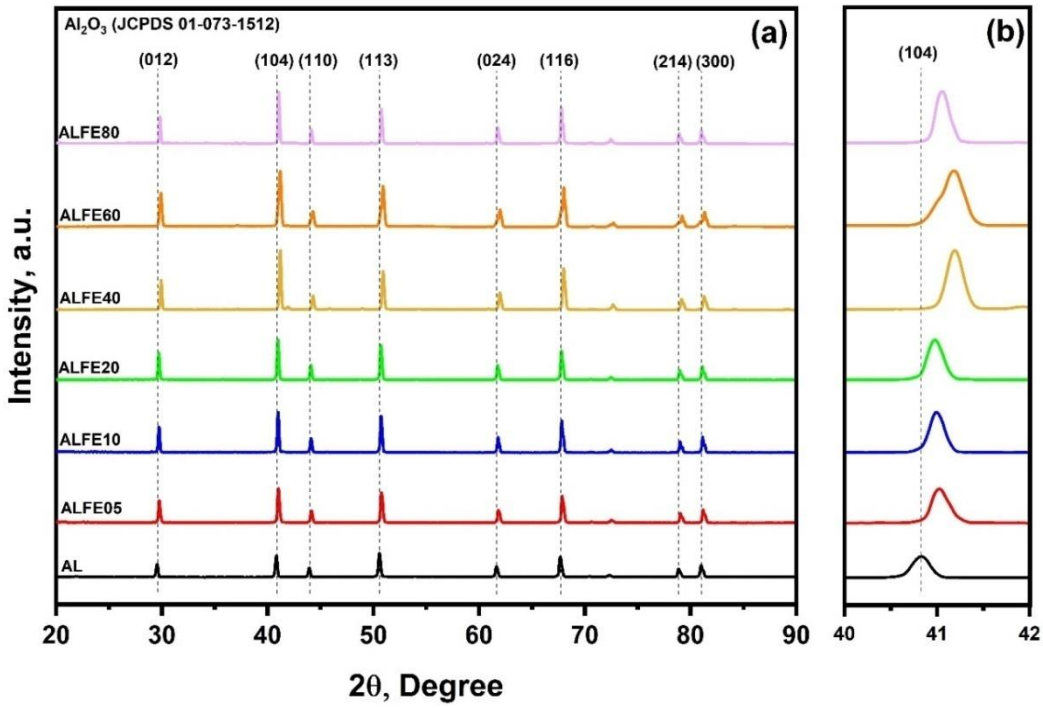

Figure 2. XRD patterns of sintered Al_2O_3 – Fe_2O_3 ceramics: (a) Complete diffractogram; (b) Amplified XRD pattern in the (104) diffraction peaks

The presence of only α-Al_2O_3 at 1400 °C, even with Fe_2O_3 additions ranging from 0.5 to 8 wt.%, aligns with the thermodynamic predictions based on the Al_2O_3–Fe_2O_3 binary phase diagram (Figure 3). This stability of the corundum phase suggests limited solubility of Fe_2O_3 in Al_2O_3 under the experimental conditions.

According to Kawasaki et al. [35], the corundum structure persists due to the very high thermal stability of α-Al_2O_3 and the strong ionic bonding within its lattice, which prevents the formation of additional phases such as $FeAlO_3$ unless the Fe_2O_3 concentration exceeds 18 wt.%. At this threshold, significant Fe^{3+} diffusion and substitution occur, leading to the formation of the $FeAlO_3$ phase with an orthorhombic structure (space group Pna21) characterized by a complex combination of hexagonal and cubic oxygen packing [36,37].

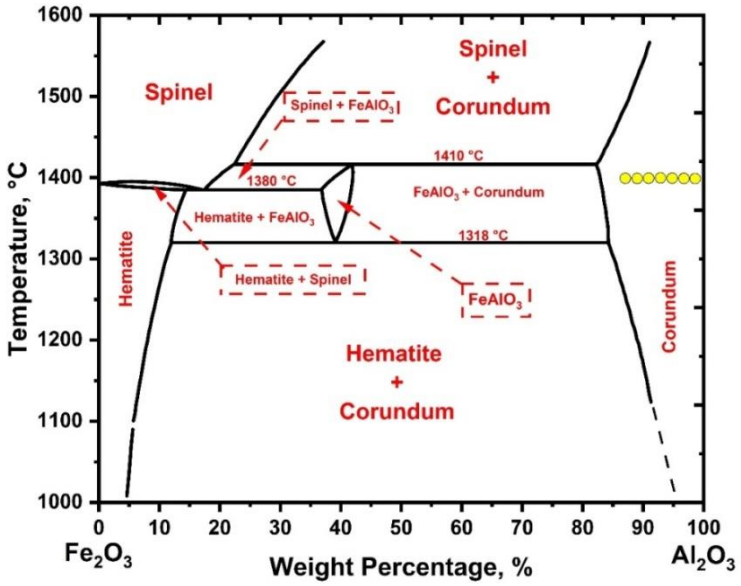

Figure 3. Phase diagram of Fe_2O_3 – Al_2O_3 compound indicating the phase of the sintered samples with yellow dots

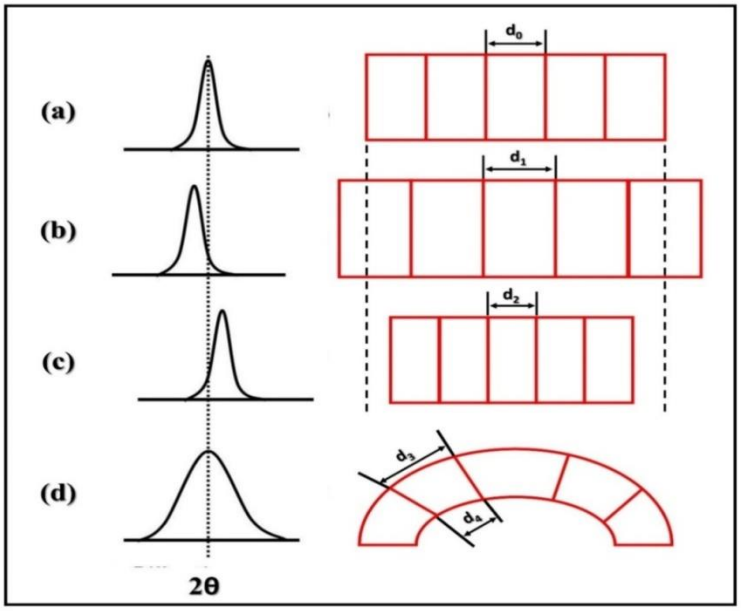

Figure 4. Diagram showing the effect of lattice strain on peak broadening and position shifts: (a) No strain at the original lattice spacing, (b) Peak shifts to lower angles when the lattice spacing is larger (d_0< d_1), (c) Peak shifts to larger angles when the lattice spacing is smaller (d_2< d_0), and (d) Peak is broadened because the peak gradually shifts from lower angles (top of the crystal: d_3) to larger angles (bottom of the crystal: d4) (d_4< d_0< d_3).

The process of $FeAlO_3$ phase formation involves Al^{3+} substitution by Fe^{3+} ions, which leads to lattice distortions and significant atomic rearrangement during sintering. This substitution process is kinetically limited at lower concentrations and temperatures due to the slow diffusion of Fe ions within the alumina matrix. Additionally, the narrow stability range of the $FeAlO_3$ phase makes its synthesis inherently challenging. The formation of a single-phase multiferroic ceramic, which could have practical applications in advanced technologies, requires precise control over the Fe_2O_3 content, temperature, and sintering conditions [37].

A closer analysis of the (104) diffraction peak, detailed in Fig.2(b), reveals significant changes in peak position, broadening, and intensity with increasing Fe_2O_3 content. These changes are attributed to microstructural effects such as lattice strain, crystallite size reduction, and local distortions caused by the Fe^{3+} substitution into the Al_2O_3 lattice. As illustrated in Figure 4, tensile and compressive lattice strains influence the d-spacing of the crystal planes, shifting the peak positions to smaller or larger 2θ values. Uniform tensile strain increases the interplanar spacing, while non-uniform strain causes asymmetry in peak broadening. The relative contributions of strain and crystallite size can be quantified by analyzing the peak width variation as a function of 1/cosθ, which highlights the significance of microstructural defects [38,39].

3.2. Crystallite size and dislocation density by scherrer analysis

The broadening of X-ray diffraction peaks typically arises from instrumental broadening, crystallite size effects, and lattice strain caused by dislocations. To separate these contributions, the instrumental broadening β_{hkl} must first be determined using a standard material like silicon. The corrected instrumental broadening is calculated using Equation 1:

$$\beta_D^2 = [(\beta_{measured}^2) - (\beta_{instrumental}^2)] \quad (1)$$

The crystallite size (CS) can then be estimated using the Scherrer equation:

$$CS = \frac{k\lambda}{\beta_D cos\theta} \quad (2)$$

Where

CS is the crystallite size (nm), k is the shape factor (k = 0.9), λ is the X-Ray wavelength (λ = 1.789 Å), θ is the Bragg angle, and β is the corrected peak width at half maximum (FWHM). The dislocation density (δ), defined as the length of dislocation lines per unit crystal volume, is calculated using Equation 3:

$$\delta = \frac{1}{D^2} \quad (3)$$

The crystallite size (CS) and dislocation density (δ) results from Table 2 reveal a nuanced relationship between Fe_2O_3 content and microstructural properties. For the base sample (AL), the crystallite size is 35.15 nm, with a dislocation density of 11.48 nm^{-2}. With the addition of 0.5 wt.% Fe_2O_3 (ALFE05), there is a slight increase in crystallite size to 35.36 nm and a corresponding decrease in dislocation density to 10.89 nm^{-2}, suggesting improved grain growth and reduced lattice imperfections.

Table 2. Crystallite size and dislocation density values obtained by Scherrer equation

GROUPS	CS (nm)	**δ** (nm^{-2})
AL	35.15	11.48
ALFE05	35.36	10.89
ALFE10	39.79	9.29
ALFE20	38.89	10.17
ALFE40	37.20	11.12
ALFE60	25.82	24.48
ALFE80	43.34	9.61

At 1 wt.% Fe_2O_3 (ALFE10), the crystallite size peaks at 39.79 nm, with a significant drop in dislocation density to 9.29 nm^{-2}, reflecting improved microstructural integrity due to a minor fluxing effect. At 2 wt.% Fe_2O_3 (ALFE20), the crystallite size slightly decreases to 38.89 nm, and dislocation density rises to 10.17 nm^{-2}, suggesting initial lattice distortions. Higher Fe_2O_3 concentrations exacerbate these effects: at 4 wt.% (ALFE40), the crystallite size drops to 37.20 nm, and dislocation density increases to 11.12 nm^{-2}; at 6 wt.% (ALFE60), crystallite size sharply declines to 25.82 nm, with dislocation density reaching 24.48 nm^{-2}, indicating severe lattice imperfections. At 8 wt.% Fe_2O_3 (ALFE80), crystallite size rebounds to 43.34 nm, and dislocation density drops to 9.61 nm^{-2}, suggesting grain coalescence and reduced distortions. Low Fe_2O_3 levels enhance structural integrity, intermediate levels introduce strain, and high levels foster recovery.

3.3. Williamson-Hall Method (W-H)

According to Williamson and Hall, for the coherent scattering region, the line broadening due to finite size and internal stress in the prepared samples can be estimated. Through mathematical manipulations, Equation 4 represents the used formula.

$$\beta_{hkl}\, cos(\theta) = \frac{k\lambda}{D} + 4\varepsilon \cdot sin(\theta) \quad (4)$$

Using Equation 4, based on the manipulation of the equation, it is possible to obtain the crystallite size by the W-H method. Figure 5 is a plot of $\beta_{hkl}\cos(\theta)$ *vs* $4\sin(\theta)$ for the samples. From the slope and intercept, both lattice strain (ε) and crystallite size were obtained. The equation above represents a model of uniform deformation in all crystallographic directions, given the high value of R in the plots. The value of ε represented by the slope in Fig.5 shows that additions of 0.5 and 1% wt.% Fe_2O_3 caused low distortions in the lattice of Al_2O_3. Additions above 2 wt.% caused a greater distortion in the crystal lattice, which may have contributed to the low mechanical performance as stated in [34].

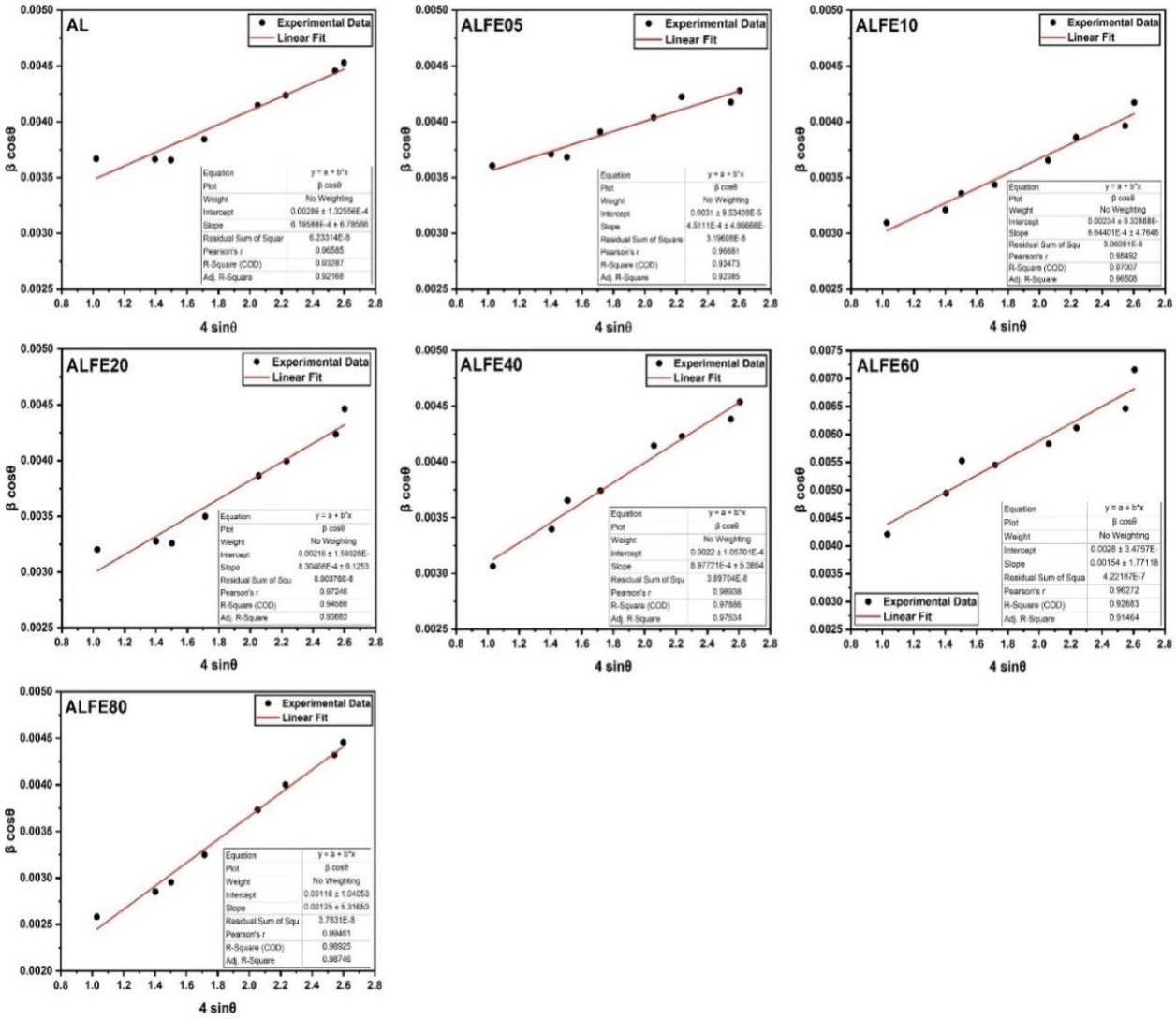

Figure 5. Williamson – Hall (W – H) plot of 4·sinθvs β·cosθ of Al_2O_3 – Fe_2O_3 ceramics

The crystallite size (CS) and lattice strain (ε) values obtained using the Williamson-Hall (W-H) method, as shown in Table 3, provide a detailed view of the microstructural behavior of alumina-based ceramics with varying Fe_2O_3 concentrations. The W-H method incorporates peak broadening effects, including internal stresses and crystal distortions, offering more reliable insights compared to simpler models.

Table 3. Crystallite size and lattice strain values obtained by Williamson-Hall method

GROUPS	CS (nm) (W-H Method)	ε
AL	58.80	0.62
ALFE05	54.25	0.45
ALFE10	71.86	0.64
ALFE20	77.85	0.83
ALFE40	76.44	0.90
ALFE60	60.06	1.54
ALFE80	144.97	1.20

The addition of Fe_2O_3 significantly influences crystallite size and lattice strain in Al_2O_3-Fe_2O_3 ceramics. For pure alumina (AL), the crystallite size is 58.80 nm. At 0.5 wt.% Fe_2O_3 (ALFE05), it decreases slightly to 54.25 nm (-7.8% compared to AL), likely due to minor structural changes. As Fe_2O_3 increases to 1 wt.% (ALFE10), crystallite size grows to 71.86 nm (+22.2%), reaching 77.85 nm (+32.4%) at 2 wt.% (ALFE20). At 4 wt.% (ALFE40), it slightly reduces to 76.44 nm (-1.8%), then drops to 60.06 nm (-21.4%) at 6 wt.% (ALFE60), suggesting structural disruptions. At 8 wt.% Fe_2O_3 (ALFE80), crystallite size surges to 144.97 nm (+146.5%), indicating relaxation and coalescence at high Fe_2O_3 levels.

Lattice strain (ε) shows an inverse trend. It decreases from 0.62 (AL) to 0.45 (-27.4%) at 0.5 wt.% Fe_2O_3, then rises progressively: 0.64 (+42.2%) at 1 wt.%, 0.83 (+29.7%) at 2 wt.%, and 0.90 (+8.4%) at 4 wt.%. At 6 wt.% Fe_2O_3, strain spikes to 1.54 (+71.1%), indicating significant distortions, before decreasing to 1.20 (-22.1%) at 8 wt.%, aligning with the large crystallite size and suggesting structural relaxation.

The Fig.6 illustrates the comparison between crystallite size values obtained using the Scherrer equation and the Williamson-Hall method for Al_2O_3 - Fe_2O_3 samples. A clear disparity in the values can be observed, with the W-H method consistently yielding larger crystallite sizes across all compositions.

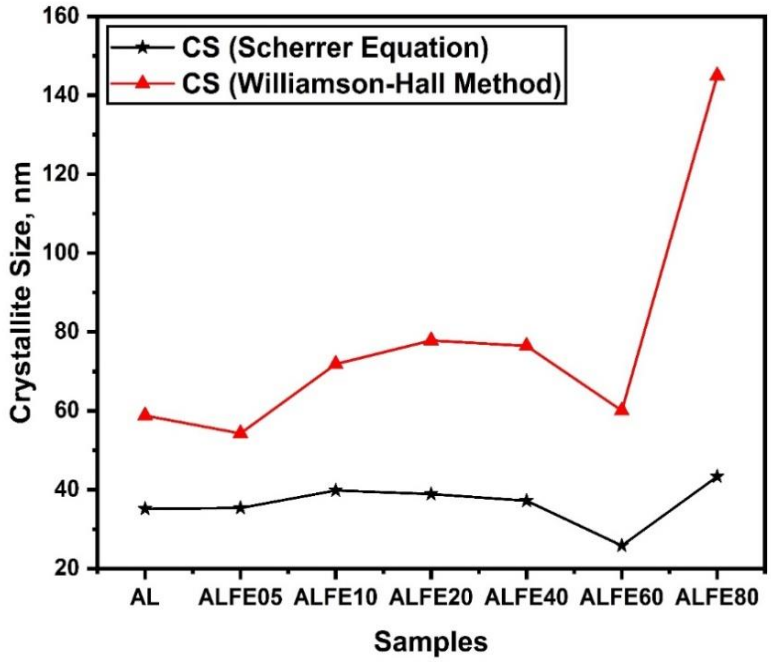

Figure 6. Comparison of Crystallite Size of Al_2O_3 - Fe_2O_3 Samples Using the Scherrer Equation and Williamson-Hall Analysis

This consistent difference arises from the distinct principles underlying the two methods. The Scherrer equation primarily considers the broadening of diffraction peaks caused by the crystallite size and assumes that broadening is solely due to this factor. It does not account for contributions from microstrain, dislocations, or other defects in the material. In contrast, the W-H method incorporates both size-induced and strain-induced broadening, offering a more comprehensive analysis of diffraction peak broadening. This additional consideration of lattice distortions and microstrain leads to the generally higher crystallite size values calculated using the W-H method.

4. CONCLUSION

In this paper, the variation of crystallite size, lattice strain, and dislocation density as a function of Fe_2O_3 content in Al_2O_3 was investigated. Fe_2O_3 addition promoted an increase in crystallite size, identified by both the Scherrer equation and W-H method, except for the addition of 6 wt.% of Fe_2O_3, which caused a reduction in crystallite size and an increase in dislocation density. Peak identification only showed the Al_2O_3 phase, without the presence of Fe_2O_3 or another phase, corroborating with the Fe_2O_3-Al_2O_3 phase diagram. Both techniques for

determination showed the same trend of crystallite size growth, although the values obtained by the W-H method were higher.

Acknowledgements

The authors Pedro Henrique Poubel Mendonça da Silveira and Marcelo Henrique Prado da Silva thank the Fundação de Amparo à Pesquisa do Estado do Rio de Janeiro (FAPERJ) for their support - grant numbers E-26/200.338/2024 and E-26/200.339/2024.

5. REFERENCES

[1] J. Baltazar, M. F. R. P. Alves, C. dos Santos, S. Olhero (2022) Reactive Sintering of Al2O3–Y3Al5O12 Ceramic Composites Obtained by Direct Ink Writing. *Ceramics*, 5, 1–12. https://doi.org/10.3390/ceramics5010001

[2] P. H. P. M. Da Silveira, T. T. da Silva, M. P. Ribeiro, P. R. R. Jesus, P. C. R. S. Credmann, A. V. Gomes (2021) A Brief Review of Alumina, Silicon Carbide and Boron Carbide Ceramic Materials for Ballistic Applications. *Acad. Let*., 1–11. http://dx.doi.org/10.20935/al3742

[3] E. Keramat, B. Hashemi (2021) Modelling and optimizing the liquid phase sintering of alumina/CaO–SiO2–Al2O3 ceramics using response surface methodology. *Cer. Int.,* 47, 3159–3172.https://doi.org/10.1016/j.ceramint.2020.09.153

[4] R. M. German, P. Suri, S. J. Park (2009) Review: liquid phase sintering. *J. Mat. Sci*., 44, 1–39. https://doi.org/10.1007/s10853-008-3008-0

[5] D. Yin, J. Wang, M. Ni, P. Liu, Z. Dong, D. Tang (2021) Fabrication of Highly Transparent Y2O3 Ceramics with CaO as Sintering Aid. *Materials*, 14, 444. https://doi.org/10.3390/ma14020444

[6] J. W. Lee, J. M. Cha, B. H. Bae, S. W. Choi, H. D. Jung, C. B. Yoon (2021) Effects of using MgO, CaO additives as sintering aid in pressureless sintering of M2Si5N8:Eu2+ (M = Ba, Sr) phosphor ceramics for amber LED automotive applications. *J. Alloy. Compd.,* 858, 157710. https://doi.org/10.1016/j.jallcom.2020.157710

[7] C. Pan, G. Zhao, S. Li, J. Wang, L. Yin, W. Song, et al. (2021) Effect of BaO-2B2O3 sintering aid on the structural and electrical properties of CaBi2Nb2O9 high-temperature piezoelectric ceramic. *J. Appl. Phys.,* 130, 244102. https://doi.org/10.1063/5.0075730

[8] P. H. P. Da Silveira, P. R. R. De Jesus, M. P. Ribeiro, S. N. Monteiro, J. C. S. De Oliveira, A. V. Gomes (2020) Sintering Behavior of AL2O3 Ceramics Doped with Pre-Sintered NB2O5 and LiF. *Mat. Sci. For.,* 1012, 190–195. https://doi.org/10.4028/www.scientific.net/MSF.1012.190

[9] K. Shan, R. Li, J. Liu (2022) Ultra-high creep resistant SiC ceramics prepared by rapid hot pressing. *J. Eur. Cer. Soc.,* 42, 1815–1821. https://doi.org/10.1016/j.jeurceramsoc.2021.11.010

[10] C. Zhang, S. Qu, W. Xi, Y. Liang, J. Zhao, T. Yu (2022) Ultra-high creep resistant SiC ceramics prepared by rapid hot pressing. *Cer. Int.,* 48, 26269–26277. https://doi.org/10.1016/j.ceramint.2022.02.090

[11] N. C. De Carvalho, J. J. De Sousa Melo, F. H. S. Sales (2022) Medidas Elétricas e Dielétricas em Cerâmicas de BaTiO3 Dopadas com SiO2 e Bi2O3 / Electrical and Dielectric Measurements in SiO2 and Bi2O3 doped BaTiO3 Ceramics. *Braz. J. Dev*., 8, 6871–6899. https://doi.org/10.34117/bjdv8n1-464

[12] A. V. Gomes, É. Lima Jr, P. R. R. De Jesus, L. F. C. Nascimento, J. L. Dos Santos, S. N. Monteiro, et al. (2020) Novel Alumina Compounds with Niobia, Silica and Magnesia for Ballistic Armor *Mat. Sci. For.,* 1012, 196–201. https://doi.org/10.4028/www.scientific.net/MSF.101.196

[13] H. P. Corado, P. H. Silveira, V. L. Ortega, G. G. Ramos, C. N. Elias (2022) Flexural Strength of Vitreous Ceramics Based on Lithium Disilicate and Lithium Silicate Reinforced with Zirconia for CAD/CAM. *Int. J. Biomater.,* 1–9. https://doi.org/10.1155/2022/5896511

[14] J. Hu, H. Li, S. Chen, W. Xiang (2022) Enhanced Fe2O3/Al2O3 Oxygen Carriers for Chemical Looping Steam Reforming of Methane with Different Mg Ratios. *Ind. Eng. Chem. Res.,* 61, 1022–1031. https://doi.org/10.1021/acs.iecr.1c03933

[15] Y. Jiang, Q. Mao, T. Ma, X. Liu, Y. Li, S. Ren (2021) Facile preparation of Fe2O3 Al2O3 composite with excellent adsorption properties towards Congo red. *Cer. Int.,* 47, 13884–13894. https://doi.org/10.1016/j.ceramint.2021.01.255

[16] L. Liu, M. R. Zachariah (2013) Enhanced Performance of Alkali Metal Doped Fe2O3 and Fe2O3/Al2O3 Composites As Oxygen Carrier Material in Chemical Looping Combustion. *Energ. Fuel.,* 27, 4977–4983. https://doi.org/10.1021/ef400748x

[17] P. H. P. M. da Silveira, A. E. Eltom, N. V. Le Sénéchal, J. L. dos Santos, A. V. Gomes, M. H. P. da Silva (2025) Evaluation of the Effect of Fe2O3 as a Sintering Additive on Densification, Microstructure, and Thermal Stability of Al2O3. *Adv. Mat. Sustain. Manuf.*, 2(1), 10005. https://doi.org/10.70322/amsm.2025.10005

[18] Z. Ma, G. Liu, Y. Lu, H. Zhang (2022) Redox performance of Fe2O3/Al2O3 oxygen carrier calcined at different temperature in chemical looping process. *Fuel*, 310, 122381. https://doi.org/10.1016/j.fuel.2021.122381

[19] Abyzov (2019) Aluminum Oxide and Alumina Ceramics (review). Part 1. Properties of Al2O3 and Commercial Production of Dispersed Al2O3. *Refract. Ind. Cer*., 60, 24–32. https://doi.org/10.1007/s11148-019-00304-2

[20] P. Bercoff, H. Bertorello (2010) Magnetic properties of hematite with large coercivity. *Appl. Phys. A*, 100, 1019–1027. https://doi.org/10.1007/s00339-010-5983-7

[21] A. Muan (1958) On the Stability of the Phase Fe2O3 .Al2O3 *Am. J. Sci.,* 256, 413–422. https://doi.org/10.2475/ajs.256.6.413

[22] A. Muan, C. Gee (1956) Phase Equilibrium Studies in the System Iron Oxide- A12O3 in Air and at 1 Atm. O2 Pressure. *J. Am. Cer. Soc*., 39, 207–214. https://doi.org/10.1111/j.1151-2916.1956.tb15647.x

[23] R. Dayal, J. Gard, F. Glasser (1965) Crystal data on FeAlO3. *Acta Crystallogr.,* 18, 574–575. https://doi.org/10.1107/s0365110x65001329

[24] Feenstra, S. Sämann, B. Wunder (2005) An experimental study of Fe-Al solubility in the system corundum-hematite up to 40 kbar and 1300 °C. *J. Petrol.,* 46, 1881–1892. http://doi.org/10.1093/petrology/egi038

[25] L. Dreval, T. Zienert, O. Fabrichnaya (2016) Calculated phase diagrams and thermodynamic properties of the Al2O3–Fe2O3–FeO system. *J. Alloy. Compd.,* 657, 192–214. https://doi.org/10.1016/j.jallcom.2015.10.017

[26] Y. Q. Cai, Z. F. Wang, L. X. Yu, J. L. Bu, R. L. Wang, R. S. Wang (2011) Effect of Molar Ratio of MgO/Al2O3 on the Performance of MgO-Al2O3-Fe2O3 Composite. *Adv. Mat. Res.,* 284–286, 242–245.https://doi.org/10.4028/www.scientific.net/AMR 284-286.242

[27] P. H. P. Silveira, A. E. Eltom, A. V. Gomes, M. H. P. Silva (2024) Sintering behavior, phase formation, physical and mechanical properties of Al2O3 – Nb2O5 ceramics produced by pressureless sintering using Fe2O3 as sintering aid. *Mat. Let.,* 359, 135966. https://doi.org/10.1016/j.matlet.2024.135966

[28] P. H. P. M. Silveira, A. E. Eltom, J. L. Santos, G. C. G. Delaqua, C. M. F. Vieira, P. R. R. Jesus, M. H. P. Silva, A. V. Gomes (2024) Addition of hematite as a sintering aid in alumina: effect of concentration on physical, microstructural and mechanical properties. *Tecnol. Met. Mat Min*., 21, 2978. http://dx.doi.org/10.4322/2176-1523.20242978

[29] Himabindu, N. S. M. P. Latha, B. R. Kanth (2021) Microstructural parameters from X-ray peak profile analysis by Williamson-Hall models; A review. *Mater. Today: Proc.,* 47, 4891–4896. https://doi.org/10.1016/j.matpr.2021.06.256

[30] J. S. Lim, F. K. Yam (2025) Structural parameters of CVD synthesized Ga2O3 nanostructures from X-ray diffraction analysis derived by Scherrer, Williamson-Hall, Size-Strain Plot and Halder-Wagner methods–A comparative study. *Physica B Condens. Matter*, 699, 416798. https://doi.org/10.1016/j.physb.2024.416798

[31] Q. Huang, C. Wang, Z. Zhou, J. Peng, Q. Shan (2025) Stress quantification in textured materials considering anisotropic crystal orientation via X-ray diffraction. *Mater. Sci. Eng. A,* 920, 147545. https://doi.org/10.1016/j.msea.2024.147545

[32] M. K. Alam, M. S. Hossain, N. M. Bahadur, S. Ahmed (2024) A comparative study in estimating of crystallite sizes of synthesized and natural hydroxyapatites using Scherrer Method, Williamson-Hall model, Size-Strain Plot and Halder-Wagner Method. *J. Mol. Struc*., 1306, 137820. https://doi.org/10.1016/j.molstruc.2024.137820

[33] Z. Cao, M. Qin, B. Jia, Y. Gu, P. Chen, A. A. Volinsky, X. Qu (2015) One pot solution combustion synthesis of highly mesoporous hematite for photocatalysis. *Cer. Int.,* 41, 2806–2812. https://doi.org/10.1016/j.ceramint.2014.10.100

[34] T. Kawasaki, T. Adachi, H. Ohfuji, Y. Osanai (2019) FeAlO3 under ultrahigh–temperature metamorphic conditions: Experimental evidence from the sillimanite–Fe2O3 and sillimanite–Fe3O4 systems. *J. Miner. Petrol. Sci.,* 114, 238–251. https://doi.org/10.2465/jmps.190509

[35] R. Saha, A. Shireen, S. N. Shirodkar, U. V. Waghmare, A. Sundaresan, C. N. R. Rao (2012) Multiferroic and magnetoelectric nature of GaFeO3, AlFeO3 and related oxides. *Solid State Commun*., 152, 1964–1968. https://doi.org/10.1016/j.ssc.2012.07.018

[36] Bhushan, S. Mukherjee, A. Basumallick, S. K. Bandopadhyay, D. Das (2008) Low temperature route to the multiferroic FeAlO3: XRD and Mössbauer characterizations. *Hyperfine Interact*., 187,101–107. https://doi.org/10.1007/s10751-008-9889-0

[37] N. S. Ramgir, Y. K. Hwang, I. S. Mulla, J. S. Chang (2006) Effect of particle size and strain in nanocrystalline SnO2 according to doping concentration of ruthenium. *Solid State Sci.,* 8, 359–362. https://doi.org/10.1016/j.solidstatesciences.2006.02.008

[38] Y. Liao (2006) Practical Electron Microscopy and Database, S.L.: S.L.

IZVOD

PROUČAVANJE VELIČINE KRISTALITA I DEFORMACIJE REŠETKE VILLIAMSON-HALL ANALIZOM U SINTEROVANOJ Al_2O_3 - Fe_2O_3 KERAMICI

Ova studija istražuje uticaj hematita (Fe_2O_3) kao pomoćnog sredstva za sinterovanje u keramici na bazi aluminijuma (Al_2O_3). Uzorci sa koncentracijama Fe_2O_3 u rasponu od 0,5 do 8 tež.% su proizvedeni I sinterovani na 1400°C. Strukturna karakterizacija uzoraka je izvršena pomoću

rendgenske difrakcije (XRD). Veličina kristalita I deformacija rešetke su izračunati pomoću Debie-Scherrer I Villiamson-Hall jednačina. Rezultati su pokazali da dodavanje Fe_2O_3 podstiče povećanje veličine kristalita u skoro svim kompozicijama, što dovodi do izobličenja u Al_2O_3 rešetki. Štaviše, povećanje veličine kristalita je dovelo do smanjenja gustine dislokacija unutar keramike. Ovaj rad doprinosi boljem razumevanju sistema Al_2O_3 – Fe_2O_3 I njegove primene u naprednim keramičkim materijalima, naglašavajući važnost pravilnog sastava u keramici ovog jedinjenja za optimizaciju svojstava ovih materijala.
Ključne reči: *Al_2O_3, Fe_2O_3, veličina kristala, XRD, Villiamson – Hall.*

Naučni rad
Rad primljen: 12.01.2025.
Rad prihvaćen: 09.04.2025.

1. Pedro Henrique Poubel Mendonça da Silveira: https://orcid.org/ 0000-0002-2651-1285
2. Jheison Lopes dos Santos: https://orcid.org/0000-0002-7075-1665
3. Alaelson Vieira Gomes: https://orcid.org/0000-0003-1651-2804
4. Marcelo Henrique Prado da Silva: https://orcid.org/0000-0002-1182-5345